Journal of CO_2 Utilization 13 (2016) 71–80

Contents lists available at ScienceDirect

Journal of CO_2 Utilization

journal homepage: www.elsevier.com/locate/jcou

Tailoring the properties of electrolyzed Ni/mesostructured silica nanoparticles (MSN) via different Ni-loading methods for CO_2 reforming of CH_4

S.M. Sidik[a], S. Triwahyono[b,*], A.A. Jalil[a,c], M.A.A. Aziz[a], N.A.A. Fatah[a], L.P. Teh[b]

[a] Department of Chemical Engineering, Faculty of Chemical and Energy Engineering, Universiti Teknologi Malaysia, 81310 UTM Johor Bahru, Johor, Malaysia
[b] Department of Chemistry, Faculty of Science, Universiti Teknologi Malaysia, 81310 UTM Johor Bahru, Johor, Malaysia
[c] Centre of Hydrogen Energy, Institute of Future Energy, Universiti Teknologi Malaysia, 81310 UTM Johor Bahru, Johor, Malaysia

ARTICLE INFO

Article history:
Received 20 August 2015
Received in revised form 29 November 2015
Accepted 15 December 2015
Available online xxx

Keywords:
Nickel-loading method
Mesostructured silica nanoparticles
Particles size
Basicity
Hydrogen production

ABSTRACT

A series of Ni/mesostructured silica nanoparticles (NiM) catalysts from an electrolyzed Ni precursor were prepared by in-situ (NiM_IS), impregnation (NiM_IM), and physical mixing (NiM_PM) methods for CO_2 reforming of CH_4. N_2 physisorption indicated that all preparation methods decreased the surface area and pore volume of the mesostructured silica nanoparticles (MSN) which may be attributed to the blockage of the pores by the deposition of NiO particles onto the MSN support. The XRD and H_2-TPR analyses indicated that the in-situ method dispersed smaller Ni^0 crystallites and exhibited a stronger metal-support interaction compared to the other methods. IR results indicated that the presence of an alkaline electrolyte during the introduction of Ni promoted sequential desilication-substitution of MSN, forming Si–O–Ni. CO_2 adsorbed IR and ESR spectroscopies showed that NiM_IS possessed a higher basicity and more defect structures compared to NiM_IM and NiM_PM, owing to the abundant silanol groups and the formation of metal-deficient Ni_2O_3. At 800 °C, the CH_4 and CO_2 conversions occur in the order of NiM_IM (CH_4 = 45.6 %, CO_2 = 52.4%) <NiM_PM (CH_4 = 60.5 %, CO_2 = 83.9 %) <NiM_IS (CH_4 = 94.3 %, CO_2 = 91.7%). The amount of carbon deposited for NiM_IM, NiM_PM and NiM_IS was 2.97%, 2.35% and 0.84%, respectively. The promoting effect of the highest catalytic activity and lowest carbon deposition for NiM_IS was related to an intimate association between better dispersion and strongly interacted Ni, as well as high basicity and concentration of surface defects in the catalyst.

1. Introduction

Catalytic CO_2 reforming of CH_4 to synthesis gas (H_2 and CO) has been proposed as one of the promising technologies for the simultaneous utilization of these two greenhouse gases. This reaction not only provides a feasible approach for resource utilization and environmental management, but also produces the chemical feedstock needed for many manufacturing processes [1]. Thus, CO_2 reforming of CH_4 has a wide application prospect. Developing a practical catalyst with high activity and good stability is not only the research hotspot of the catalyst field, but also the key of achieving CO_2 reforming of CH_4 for commercialization. Current research results indicate that noble metal catalysts have good activity and carbon deposition resistance to the reforming reaction [2]. However, Ni has drawn remarkable attention in this area, owing to its wider availability and lower cost. For the current research situation, Ni-based catalysts easily lose their activity, because of serious carbon deposition [3].

There are two main properties of a catalyst that affect carbon deposition, that is, surface structure and surface basicity. Generally, there are two major techniques that have been highlighted for improving the catalytic activity of this catalyst: (i) increasing the surface area of the metal active sites by synthesizing nano-sized materials and (ii) adding a support, such as silica, alumina, metal oxide, and so forth, to improve the dispersion of the metal and to increase the basicity of the catalyst [4,5]. In parallel with this, we have successfully synthesized Ni supported on mesostructured silica nanoparticles (MSN) for CO_2 reforming of CH_4 [6]. We found that this catalyst showed appreciable activity and stability compared to Ni/MCM-41, owing to the presence of interparticles pores that promoted a better reducibility of Ni and basicity of the catalyst. However, the incorporation mechanism of Ni into MSN is not well reported.

* Corresponding author. Fax: +60 7 5536080.
E-mail addresses: sugeng@utm.my, sugengtw@gmail.com, sugeng@ibnusina.utm.my (S. Triwahyono).

http://dx.doi.org/10.1016/j.jcou.2015.12.004
2212-9820/

Owing to this advantage, an extension of this study is worth pursuing.

It is well known that methodologies of promoted catalyst preparation have a significant effect on the physicochemical properties of catalysts and their catalytic performance [7]. In our previous study, we successfully synthesized several nano-sized particles of ZnO, CuO, and α-FeOOH supported on silica by a simple electrochemical method [8–11]. Their outstanding uses as photocatalysts in the photodegradation of organic pollutants as well as in isomerization encouraged further applications of this method for designing various types of catalysts for various applications. Recently, an electrolyzed Ni catalyst also showed better catalytic performance compared to the salt-derived Ni catalyst in CO_2 reforming of CH_4 [6]. Besides shortening the conventional synthesis time, this method can also be carried out under mild conditions without using strongly acidic conditions, hydrothermal treatment, higher temperature, and/or reactive compounds.

Therefore, in this study, we further explored the effect of Ni-loading method of the electrolyzed Ni precursor onto MSN using three methods, which is in-situ electrolysis (IS), impregnation (IM), and physical mixing (PM). Subsequently, their physicochemical properties were interpreted using MP-AES, XRD, N_2 adsorption, TEM, H_2-TPR, IR-KBr, CO_2 adsorbed IR, ESR, and TGA analyses. The relationship between the effect of the Ni-loading method and the catalytic activity in CO_2 reforming of CH_4 was investigated through a fixed bed continuous flow reaction. Depending on the preparation method used, different species and different Ni sizes were observed with variation in the reducibility and concentration of basic and structure defects. A new structural model for NiM_IS was proposed on the basis of the literature, characterizations and catalytic testing results. A relationship between these features and the catalytic performance was also discussed.

2. Experimental

2.1. Synthesis of mesoporous silica nanoparticles (MSN)

MSN was prepared by co-condensation and sol–gel method as previously reported [12,13]. In brief, the cetyltrimethylammonium bromide (CTAB, Merck), ethylene glycol (EG, Merck) and ammonium (NH_4OH, QRec) solution were dissolved in 700 mL of double distilled water with the following mole composition of CTAB:EG:NH_4OH:H_2O = 0.0032:0.2:0.2:0.1. After vigorously stirring for about 30 min at 50 °C, 1.2 mmol tetraethylorthosilicate (TEOS, Merck) and 1 mmol 3-aminopropyl triethoxysilane (APTES, Merck) were added to the clear mixture to give a white suspension solution. This solution was then stirred for another 2 h at 80 °C, and the as-synthesized MSN sample was collected by centrifugation at 20,000 rpm. The as-synthesized MSN was dried at 110 °C and calcined at 550 °C for 3 h to form surfactant-free MSN. Complete removal of the surfactant was verified by means of infrared spectroscopy, which did not reveal the presence of any residual organic species.

2.2. Preparation of Ni supported on MSN (NiM) catalysts

In this study, three types of preparation methods, in-situ electrolysis (IS), impregnation (IM) and physical mixing (PM) were carried out. For the in-situ electrolysis method, a 10 mL DMF solution was added to a one-compartment cell fitted with a platinum (Pt) plate cathode (2 cm × 2 cm) and a nickel (Ni) plate anode (2 cm × 2 cm) containing TEAP, naphthalene and MSN. Naphthalene was used as a mediator in the system to produce radical anions, which then reduced the nickel cations to give smaller nickel nanoparticles [14]. Then, the electrolysis was conducted at a constant current of 480 mA cm^{-2} and 0 °C under a N_2 atmosphere under continuous stirring. The desired Ni content supported on the MSN and the time required for complete electrolysis was calculated based on the Faraday's law of electrolysis, as shown in the following equation;

$$n = \left(\frac{It}{F}\right)\left(\frac{1}{z}\right) \quad (1)$$

where n is the number of moles of Ni, I is the constant current of electrolysis (A), t is the total time the constant current was applied (s), F is Faraday's law constant (96,487C mol^{-1}), and z is the valence number of ion of the substance (electron transferred per ion). The number of moles of Ni required was calculated based on the total time, t of the electrolysis. For example, 1137 s is the time required to produce 5 wt% of Ni in 1.5 g MSN. After electrolysis, the solvent was removed before being dried overnight at 110 °C and calcined for 3 h at 550 °C to give a dark grey colored NiM_IS catalyst. For the impregnation and physical mixing methods, a required amount Ni was firstly prepared using electrolysis procedure as describe above. After the electrolysis, the electrolyzed Ni solution was added into MSN for incipient wetness impregnation process at 80 °C. Then, the product was dried overnight at 110 °C and calcined for 3 h at 550 °C, and finally, a light green colored NiM_IM catalyst was obtained. For the physical mixing method, the electrolyzed Ni solution was directly subjected for drying at 80 °C before being dried overnight at 110 °C and calcination at 550 °C for 3 h. As a result, a black NiO powder was obtained. Finally, a desired amount of black NiO was physically mixed with MSN and calcined for 3 h at 550 °C to give a dark grey colored NiM_PM catalyst. In this study, Ni loading of NiM catalysts was adjusted at 5 wt%. In order to determine the amount of Ni in the NiM catalysts, the corresponding catalysts were dissolved in HF solution before subjected to MP-AES analysis. It was found that approximately 5 wt% Ni was successfully loaded into the NiM catalysts (Table 1).

2.3. Characterization

The elemental analyses of Ni in the catalysts were determined by microwave plasma-atomic emission spectrometer (MP-AES) using 4100 MP-AES Agilent Technologies model 98000A. The crystalline structure of the catalysts was determined with X-ray diffraction (XRD) recorded on powder diffractometer (Bruker Advance D8, 40 kV, 40 mA) using a Cu Kα radiation source in the range of 2θ = 1.5–80^0. The crystallite size of NiO and metallic Ni ($d_{Ni}{}^0$) was calculated by means of the Scherrer equation:

$$d_{NiO} = \frac{0.9\lambda}{B\cos\theta} \quad (2)$$

where λ is the X-ray wavelength corresponding to Cu-Kα radiation (0.154 nm), B is the broadening (in radians) of the NiO and Ni^0 reflection at 43.3 and 44.6^0, respectively and θ is the angle of diffraction corresponding to the peak broadening. Transmission electron microscopy (TEM) was carried out using a JEOL JEM-2100F microscope. The samples were ultrasonically dispersed in acetone and deposited on an amorphous, porous carbon grid. Nitrogen adsorption–desorption isotherms were used to determine the

Table 1
Electrolysis time, contact time between Ni solution and MSN, and the amount of Ni detected in MSN for NiM_IS, NiM_PM and NiM_IM catalysts.

Catalysts	Electrolysis time (min)[a]	Contact time between Ni solution and MSN (min)	Ni detected in catalyst (%)[b]
NiM_IS	19	139	4.97
NiM_PM	19	–	5.01
NiM_IM	19	120	4.98

[a] Calculated based on Faraday's law.
[b] Ni detected by MP-AES.

textural properties at liquid nitrogen temperatures using a Beckman Coulter SA 3100 Surface Area Analyzer. Prior to measurement, all of the catalysts were outgassed at 110 °C for 3 h before being subjected to N_2 adsorption at −196 °C. H_2-TPR experiments were carried out using Micromeritics Chemisorb 2720 Pulse Chemisorption in 10% H_2/Ar at 10 °C min^{-1}. H_2 chemisorption was measured to investigate the Ni dispersion and Ni surface area of the catalysts. Prior to the chemisorption, 30 mg of the catalyst was reduced with pure H_2 (20 mL min^{-1}) at 850 °C for 1 h. The amount of hydrogen uptake was determined by injecting mixed gas (10% H_2/Ar) periodically into the reduced catalyst. The Ni dispersion and Ni surface area were calculated by assuming that one hydrogen atom occupies one Ni atom. Fourier Transform Infrared (FTIR) measurements were carried out using Agilent Technologies Cary 640 FTIR Spectrometer. To identify the chemical functional groups present in the catalysts, the catalyst was finely ground and dispersed into KBr powder-pressed pellets with a ratio of 1 mg catalyst/100 mg KBr. For the activation spectra, the catalyst was prepared as a self-supported wafer and placed in a high-temperature stainless steel cell with CaF_2 windows before subjected to the FTIR measurement. The CO_2 adsorbed IR was carried out at room temperature for 30 min after reduction in H_2 stream (15 mL min^{-1}) at 400 °C for 1 h, followed by outgassing at 400 °C for 1 h. All spectra were recorded at room temperature with a spectral resolution of 5 cm^{-1} with five scans. In order to compare the surface coverage of the adsorbed species between different wafer thicknesses, all spectra were normalized using the overtone and combination vibrations of the lattice between 2100 and 1550 cm^{-1} [8]. All ESR spectra were recorded using a JEOL JES-FA100 ESR spectrometer at 30 °C. The carbon content was determined by thermogravimetric analysis (TGA) using a PerkinElmer TGA7 Thermogravimetric Analyzer from room temperature to 900 °C at a heating rate of 10 °C min^{-1}.

2.4. Catalytic testing

Catalytic CO_2 reforming of CH_4 were performed in a fixed-bed, continuous flow reactor at 300–800 °C. Prior to the reaction, 0.2 g of the catalyst was charged into an ID 4 mm quartz tube, and then it was subjected to O_2 treatment (O_2 = 50 mL min^{-1}) at 850 °C for 1 h, followed by H_2 reduction (H_2 = 50 mL min^{-1}) at 850 °C for 3 h. Then, the reactor was cooling down to a reaction temperature under N_2 stream. CO_2 and CH_4 were mixed at a stoichiometric ratio of 1:1 and N_2 was added as an internal standard. The feedstock with space velocity around 15,000 mL $h^{-1}g_{cat}^{-1}$ was passed over the activated catalyst and the products were analyzed using online 6090N Agilent Gas Chromatograph equipped with Carboxen 1010 packed column and TCD detector. The rates of CO_2 and CH_4 conversions and TOF values of CH_4 conversion were calculated based on the following equations, respectively;

$$\text{Rate of conversion} = \frac{[\text{mole}]_{in} - [\text{mole}]_{out}}{\text{gof catalyst} \times \text{time}} \quad (3)$$

$$\text{TOF} = \frac{[\text{mole } CH_4]_{in} - [\text{mole } CH_4]_{out}}{\text{moleofactiveNi} \times \text{time}} \quad (4)$$

3. Results and discussion

3.1. Characterization

3.1.1. XRD analysis

Fig. 1 shows the XRD patterns of the MSN and NiM catalysts prepared by different preparation methods. From the small angle XRD patterns (Fig. 1A), three peaks were observed for 2θ = 1.5–5.0°, with the most intense signal corresponding to (1 0 0) diffraction followed by two well-resolved (1 1 0) and (2 0 0) diffraction peaks. This suggested that all of the synthesized materials have a highly ordered 2D hexagonal mesoporous structure (p6mm). The intensity of these peaks decreased upon the introduction of Ni, suggesting partial blocking of the mesoporous structure and distortion of the hexagonal arrangement of the catalysts [15]. The effect becomes more prominent for NiM_IS, which may be attributed to the greater interactions between the Ni particles and MSN during in-situ electrolysis. Wide angle XRD patterns (Fig. 1B) of the NiM catalysts showed diffraction peaks for NiO at 2θ = 37.1, 43.3, 62.7, 75.1, and 79.1°, with the highest intensity observed for the NiM_IM catalyst, implying the presence of larger NiO crystallites in the catalyst. Several peaks were also observed for NiM catalysts at 2θ = 44.7 and 52.0, indicating the presence of Ni^0 on the catalyst surface, particularly for NiM_IM and NiM_PM catalysts. The XRD patterns of NiM catalysts after reduction are shown in Fig. 1C. The diffraction peak belonging to NiO was not detected in the reduced catalysts, indicated that Ni was completely reduced and mainly existed as Ni^0. A measurement of the NiO and Ni^0 crystallite size was carried out based on the peak width at half maximum using the characteristic peak at 43.3 and 44.6°, respectively. Despite the higher temperature involved in the reduction treatment, little sintering were observed for the

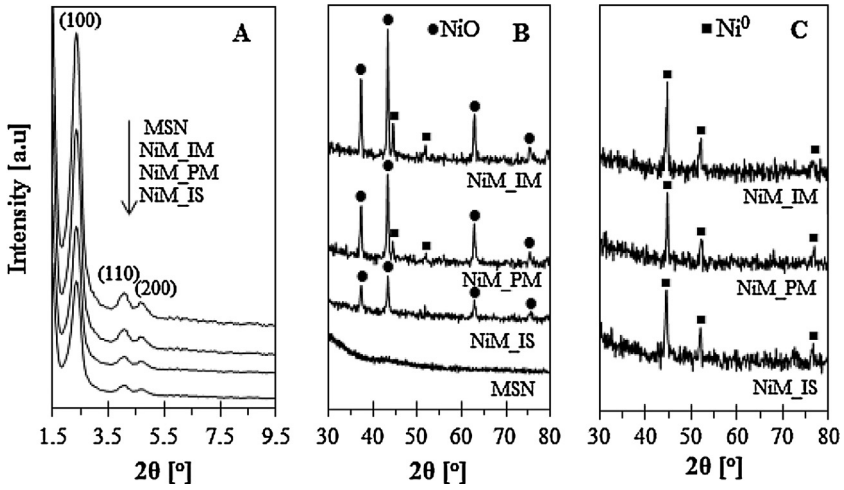

Fig. 1. (A) Low and (B) wide angle XRD patterns of fresh and (C) reduced MSN, NiM_IS, NiM_PM and NiM_IM catalysts.

Table 2
The properties of MSN, NiM_IS, NiM_PM and NiM_IM catalysts.

Catalysts	Surface area ($m^2 g^{-1}$)	Pore volume ($cm^3 g^{-1}$)	Average pore (nm)[a]	d_{NiO} (nm)[b]	d_{Ni^0} (nm)[c]	d_{Ni^0} (nm)[d]	Ni dispersion (%)[e]	Ni surface area ($m^2 g^{-1}$)[e]
MSN	894	0.978	2.58	–	–	–	n.a	n.a
NiM_IS	442	0.585	2.21	5.63	8.15	15.3	11.3	38.8
NiM_PM	686	0.735	5.33	6.10	12.6	22.7	9.70	33.2
NiM_IM	149	0.557	14.8	12.1	19.7	29.4	8.40	28.7

[a] Average pore size calculated obtained from BJH.
[b] The crystallite size of NiO in the fresh catalyst calculated from XRD using Scherer equation.
[c] The crystallite size of Ni^0 in the reduced catalyst calculated from XRD using Scherer equation.
[d] The crystallite size of Ni^0 in the spent catalyst calculated from XRD using Scherer equation.
[e] Determined using H_2 chemisorption.

catalysts as revealed by the increment in the size of Ni particles as shown in Table 2. The calculated Ni particle sizes for NiM_IS, NiM_PM, and NiM_IM catalysts were increased from 5.63, 6.10, and 12.1 nm to 8.15, 12.6, and 19.7 nm, respectively. From this result, it was observed that NiM_PM suffered a higher sintering degree, which may be due to the weaker metal-support interaction presence in the catalyst. In fact, the addition of Ni by in-situ electrolysis leads to the formation of smaller Ni^0 particles, resulting from higher dispersions of the Ni particles on the surface of the NiM_IS catalyst.

3.1.2. Morphologies and particle size analysis

The morphologies and particle size distributions of the catalysts were investigated using TEM, as shown in Fig. 2. It was observed that the hexagonal order of the MSN had been partially distorted for all NiM catalysts. The small distortion can be explained by the coverage of the NiO particles over the MSN surface that led to difficulties in observation by TEM. Besides, the greater distortion in NiM_IM and NiM_IS can be explained by a structure rearrangement in the catalysts, owing to the formation of new Si—O—Ni bonds replacing the Si—OH bonds [9]. The presence of NiO particles in the NiM catalysts was observed by the occurrence of small spots with darker contrast areas in Fig. 2. The EDX analysis recorded for the red square area further confirmed that the nanoparticles were NiO. The NiM_IS catalyst showed the deposition of the smallest NiO particles, which were in the range of 1–7 nm size, whereas NiM_PM was composed of medium-sized NiO particles in the range of 3–10 nm. For the NiM_IM catalyst, larger NiO particles and some agglomerates with sizes of 7–15 nm were observed. The average sizes of the NiO particles were determined by measuring the projected areas of 100 individual particles in the TEM image and calculating the equivalent diameter [16]. The average size of NiO crystallites for NiM_IS, NiM_PM, and NiM_IM were 5.62, 6.13, and 12.5 nm, respectively, which are closed to the value calculated from the Scherrer equation, as shown in Table 2. In accordance with the XRD results, it can be concluded that the size of NiO particles can be tailored by using different Ni-loading methods. It is believed that this will lead to different degrees of metal dispersion as well as different metallic surface areas, which strongly affect the catalytic activity.

3.1.3. N_2 adsorption–desorption analysis

To further investigate the mesoporous structure and porosity of NiM catalysts, the N_2 adsorption–desorption isotherms were studied, as shown in Fig. 3. The isotherm of the MSN exhibited a type IV isotherm curve with a H4-type hysteresis loop [17]. According to the IUPAC classification, the MSN represent a mesoporous material with a slit-like pore structure. The sharp inflections at $P/P_o = 0–0.03$ and 0.85–1 observed in the isotherm indicate the presence of micropores and interparticles voids in the

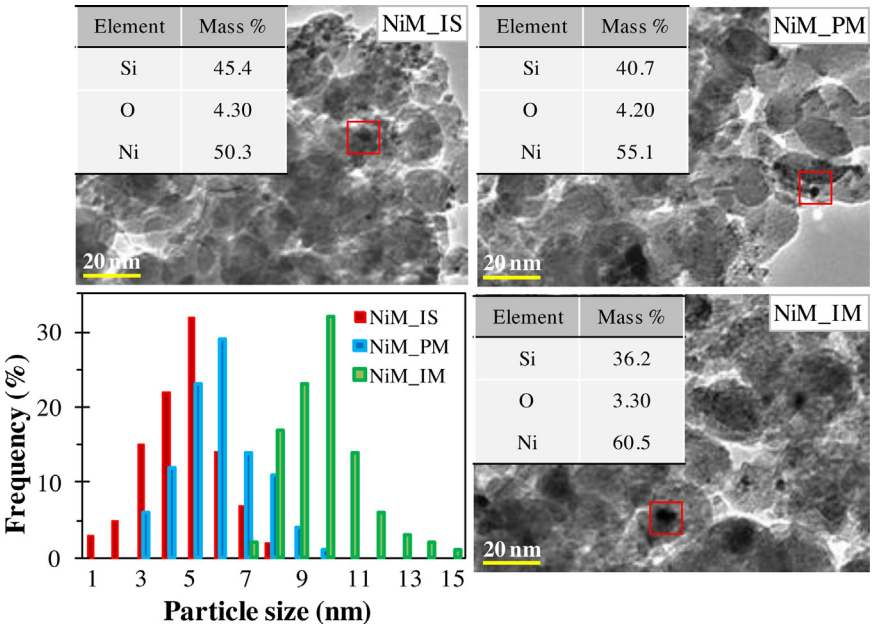

Fig. 2. TEM images and particle size distributions of NiM_IS, NiM_PM and NiM_IM catalysts.

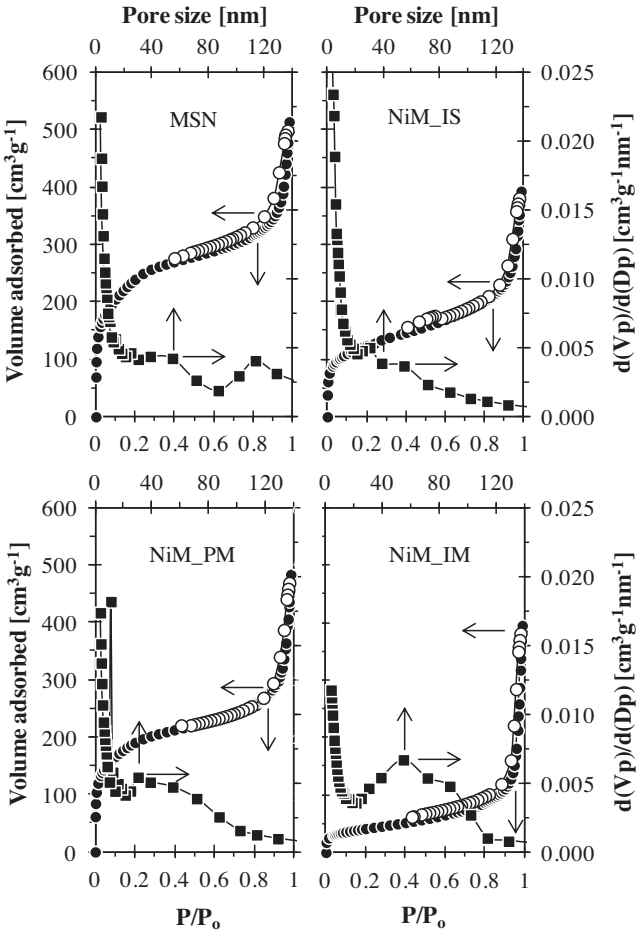

Fig. 3. N_2 adsorption (●)—desorption (○) pattern and pore size distribution (■) of MSN, NiM_IS, NiM_PM and NiM_IM catalysts.

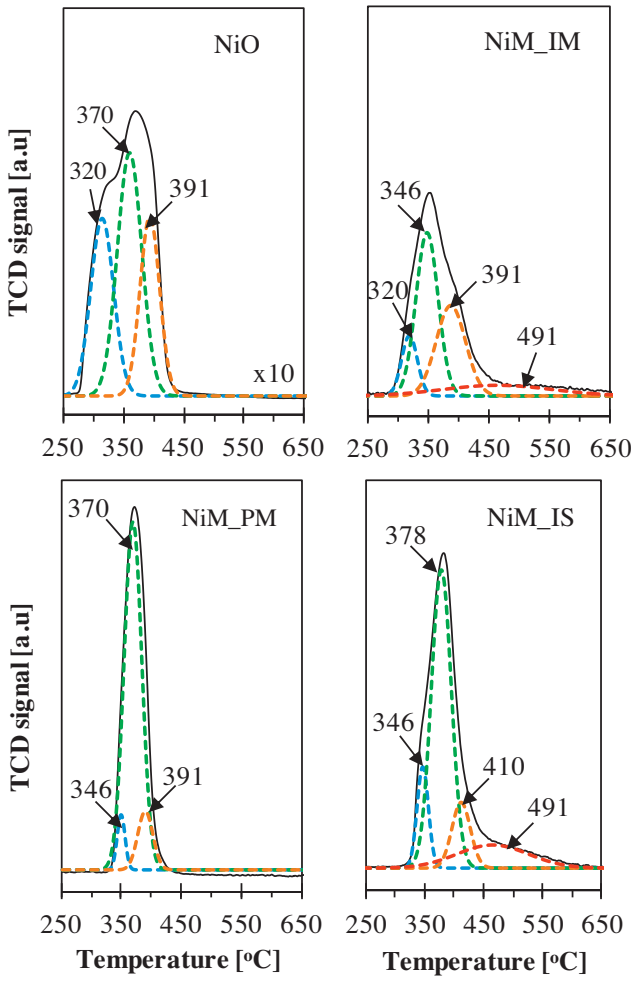

Fig. 4. H_2-TPR profiles of NiO, NiM_IM, NiM_PM and NiM_IS catalysts. The dotted line represents the Gaussian peaks.

catalysts, respectively. When Ni was introduced into the MSN, the isotherm and hysteresis loop were similar to that of parent MSN, indicating a similar mesoporous structure. Based on the summarized textural properties in Table 2, the addition of Ni by physical mixing, in-situ, and impregnation methods decreased the surface area and pore volume of the MSN from 894 to 686, 442, and 149 $m^2 g^{-1}$, and from 0.978 to 0.735, 0.585, and 0.557 $cm^3 g^{-1}$, respectively. Upon the introduction of Ni, the microporosity of all catalysts decreased, especially for NiM_IS and NiM_IM, indicating the partial blockage of the micropores by deposition of NiO particles [18]. In addition, the deposition of NiO also considerably blocked the interparticles voids of NiM_IS and, consequently, decreased the average pore size from 2.58 to 2.21 nm. On the contrary, there was a remarkable increase in the intensity of the interparticles voids of the NiM_PM and NiM_IM catalysts suggesting that the deposition of NiO particles on the catalyst surface had contributed to the formation of new pores in the size range of 40–80 nm, as shown in the pore size distribution (Fig. 3). The average pore sizes of the NiM_PM and NiM_IM catalysts were increased from 2.58 to 5.33, and 14.8 nm, respectively. An appreciable decrease in surface area and pore volume of NiM_IS and NiM_IM compared to NiM_PM is likely caused by the distortion of the silica framework in the MSN accompanied by the substitution of Ni ions into the framework. However, the formation of larger NiO particles in NiM_IM compared to NiM_IS further decreased the surface area and pore volume of the catalysts.

3.1.4. Reducibility study

Fig. 4 shows the TPR profiles for NiO and NiM catalysts. The profile of the MSN shows no hydrogen consumption at the studied temperature, indicating that no reduction occurs (figure not shown). The reduction profile of NiO shows broad hydrogen consumption between 250 and 450 °C. This profile can be deconvoluted into three peaks centered at 320, 370, and 391 °C, which are ascribed to the reduction of large Ni_2O_3, small Ni_2O_3, and small NiO particles, respectively [19]. The NiM_IM catalysts presented different reduction profiles to that of NiO, with an absence of the peak at 370 °C and an emergence of a new peak at 346 °C corresponding to large Ni_2O_3 weakly interacting with the MSN. Notably, NiM_PM and NiM_IS exhibited three similar peaks at 346, 370 and 391 °C. However, two reduction peaks of NiM_IS shifted towards a higher temperature, from 370 to 378 °C and 391 to 410 °C. It was anticipated that smaller Ni particles bound to the support surface were more difficult to reduce than the larger particles for which the interaction between NiO species and the support surface is rather weak [20]. Besides, it was observed that the NiM_IM and NiM_IS catalysts have an additional broad peak centered at 491 °C, indicating the reduction of highly dispersed Ni^{2+} that are strongly interacted with the MSN [21]. The higher reduction temperature might originate from the stronger interaction (Si-O-Ni) between Ni and MSN during the catalyst preparation steps [22]. Based on these results, the reducibility of NiM catalysts decreased in the order of NiM_PM > NiM_IM > NiM_IS. This attribution coincides with the conclusion drawn by Turlier et al.

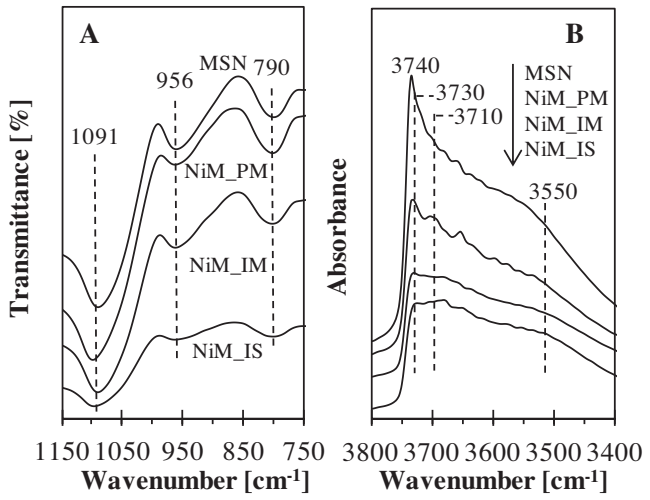

Fig. 5. (A) FTIR spectra of KBr and (B) activated MSN, NiM_IS, NiM_IM and NiM_PM catalysts.

[23] who reported that the catalysts with a larger degree of reduction showed smaller Ni dispersion. Comparing the profiles of the NiM catalysts, it was found that different Ni oxide phases were formed on the surfaces of the MSN. A larger amount of total H_2 consumption for the NiM_IS and NiM_PM indicated that the majority of the Ni species present in the catalysts had a higher oxidation state compared to the Ni in the NiM_IM catalyst, because a greater amount of H_2 is required to reduce Ni_2O_3 (Ni^{3+}) to Ni^0 compared to NiO (Ni^{2+}) to Ni^0. This finding correlates well with the visual observation of the catalyst. In this study, the Ni oxide prepared using the electrolysis method is black in color, which can be assigned to Ni_2O_3 species [24]. However, due to the presence of NiO peak in the XRD pattern, it can be suggested that the prepared Ni oxide is consisted of a mixture of NiO and Ni_2O_3. As for the NiM_PM and NiM_IS catalysts, their dark grey appearance indicates a higher amount of the Ni_2O_3 phase were presented in the catalysts compared to the NiM_IM. Whereas, for NiM_IM, its light green color suggests that most of the Ni particles are in the form of NiO. Since no obvious signal for Ni_2O_3 was found in the XRD patterns (Fig. 1B), it is suggested that Ni_2O_3 is highly dispersed on the NiM_PM and NiM_IS catalysts [25].

3.1.5. Spectroscopic study

FTIR spectroscopy in the skeletal region at 1150–750 cm^{-1} (Fig. 5A) was used to study the interaction of the atoms and structure of the catalysts upon the introduction of Ni using various preparation methods. Typical FTIR bands from the siliceous Si—O—Si material were observed for MSN and NiM catalysts. The band at approximately 1091 cm^{-1} was ascribed to the asymmetric Si—O—Si stretching vibration. Two weaker bands at approximately 956 and 790 cm^{-1} were attributed to Si—OH and symmetric Si—O—Si stretching vibrations, respectively [11]. The spectrum of NiM_PM is similar to that of the MSN and remained unchanged upon the addition of Ni, indicating that the introduction of Ni by physical mixing did not affect the Si—O—Si stretching and no interaction was formed between Ni and the MSN. The introduction of Ni into the MSN decreased both of Si—O—Si stretching vibration intensities at 1091 and 790 cm^{-1} for the NiM_IM and NiM_IS catalysts, indicating the occurrence of desilication, owing to the presence of ammonium salt solution during the in-situ electrolysis and impregnation of the catalysts [10]. A greater loss in the peaks intensity of NiM_IS was possibly attributed to a longer contact time between the MSN and the solution during the in-situ preparation of the catalyst, thus triggering greater desilication to occur. The intensity of the (1 0 0) peak in the XRD pattern for NiM_IS was drastically reduced compared to MSN, NiM_PM, and NiM_IM, confirming that the desilication is controlled by the contact time of the catalyst with the ammonium salt solution. Moreover, both NiM_IM and NiM_IS showed a decreasing trend in the peak intensity at 956 cm^{-1}, particularly for the latter, suggesting that replacement of the –OH group by O-metal ions probably occurred and led to the formation of Si—O—Ni. This result is in agreement the H_2-TPR analysis, in which NiM_IM and NiM_IS showed broad reduction peaks centered at 491 °C, owing to the reduction in Ni strongly interacting with MSN originating from Si—O—Ni.

The spectra of hydroxyl groups in activated MSN and NiM catalysts are presented in Fig. 5B. Activated MSN and NiM catalysts possessed intense bands at 3740 cm^{-1} with a shoulder at 3710 cm^{-1} and a broad peak centered at about 3550 cm^{-1}. The bands at 3740 and 3710 cm^{-1} are unambiguously assigned to terminal and internal silanol groups, respectively [26]. The broad absorbance centered at 3550 cm^{-1} is indicative of the presence of H-bonded hydroxyl groups. The addition of Ni decreased the intensity of the terminal and internal silanol bands, and also shifted the terminal silanol band at 3740 cm^{-1} to 3730 cm^{-1}. In addition, the peak associated with hydrogen bonded silanol groups at 3550 cm^{-1} was intensified upon the addition of Ni. These may be related to the formation of surface defects resulting from the desilication and interaction of Ni with terminal and internal silanol groups to form Si—O—Ni. The degree of interaction of Ni with MSN is dependent on the preparation method. It is believed that this will lead to different capacities of Si—O—Ni bonds, basicity as well as surface defects, which will affect the catalytic activity of NiM catalysts.

Based on the above characterization data and literature basis, probable reaction pathways and structure of the catalysts are proposed in Fig. 6. Firstly, electrolysis of a DMF solution with a Pt

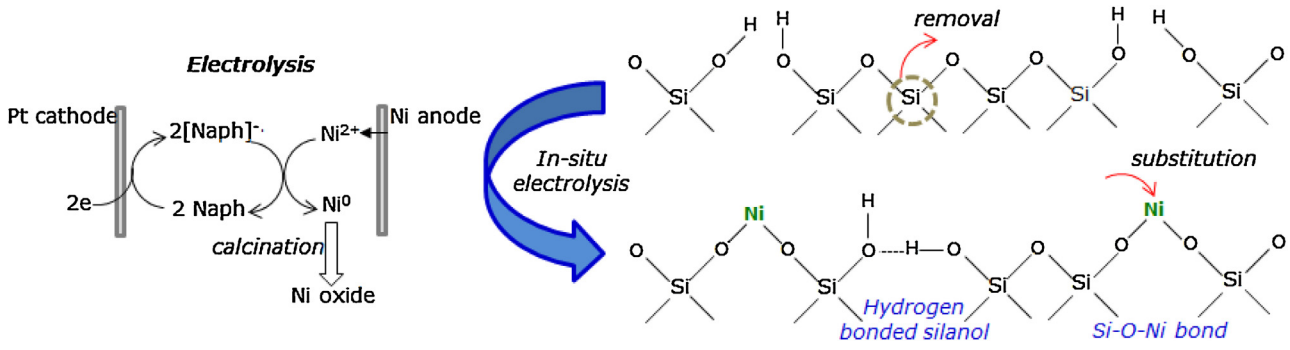

Fig. 6. Proposed reaction pathways for the formation of NiM_IS catalysts.

cathode and a Ni anode results in anodic dissolution of Ni metal to give Ni^{2+}. At the same time, the presence of ammonium salt (TEAP) solution in the electrolysis system allowed desilication to occur, thus increasing the number of perturbed and hydrogen-bonded silanol groups, as confirmed by XRD and FTIR analyses. In addition, a decrease in the numbers of external Si—OH groups at 956 cm^{-1} upon the addition of Ni suggested the subsequent substitution of the terminal and internal silanol groups with some of the Ni^{2+} to form Si—O—Ni bonds. In parallel, the one-electron reduction of naphthalene molecules occurred at the cathode to give radical anion naphthalene, which was evidenced by the appearance of a dark green color on the surface of the cathode. The remaining Ni^{2+} was then reacted with naphthalene radical anions to give zero-valence Ni, Ni^0. Upon calcination of the final catalysts, Ni^0 was oxidized to NiO and Ni_2O_3, which were detected by XRD and H_2-TPR analyses. The stronger interactions between the Ni particles and MSN during in-situ electrolysis minimized the agglomeration of Ni, which resulted in smaller and uniform NiO particles. In the case of NiM_PM and NiM_IM, deposition of Ni takes place during drying/calcination. As this deposition method lacks the strong interaction with well-dispersed surface sites, the large average size of the particles is not surprising [27].

3.1.6. Oxygen defects and basicity studies

In general, ESR spectroscopy is used for studying materials with unpaired electrons. In the present work, this technique was used to study the occurrence of defect structures in MSN and NiM catalysts. All NiM catalysts showed similar ESR signals at $g = 2.45$ (Fig. 7A), which is related to the presence of cationic defects on the surface [28]. The introduction of Ni into MSN by in-situ electrolysis, physical mixing and impregnation methods increased the peak intensities. Notably, the highest peak intensity was observed for NiM_IS, followed by NiM_PM and NiM_IM. This phenomenon may be related to the presence of non-stoichiometric Ni_2O_3 in the catalysts. In non-stoichiometric Ni_2O_3 compounds, a small percentage of Ni atoms are deficient or too many oxygen atoms are packed into a perfect lattice framework, which results in flaws and defect structures. Based on the proposed reaction pathways of the electrosynthesized catalysts, some Ni^{2+} reacted with external Si—OH to form Si—O—Ni. However, the excess Ni^{2+} was reduced to Ni^0 when in contact with naphthalene radical anions. After that, the Ni^0 was further oxidized to form Ni oxide upon the calcination of this catalyst. From H_2-TPR analysis, we found that a mixture composition of Ni_2O_3 and NiO in the NiM_IS and NiM_PM was present, which contributed to the dark grey color. However, for NiM_IM, the light green appearance suggested that NiO is the major compound. Although NiO is generally the only stable oxide formed in air or oxygen, it has been proposed that Ni_2O_3 may exist at low temperatures and the formation of Ni_2O_3 has been related to the reaction of oxygen with the surface of NiO [29].

CO_2 is a probe for the basicity analysis of solids, as it forms carbonate-like species with basic oxygen atoms. In this study, in-situ FTIR spectra of adsorbed CO_2 were used to illustrate the states of adsorbed CO_2 species that interacted with the basic sites on the surface of MSN and NiM catalysts. Fig. 7B displays the spectra of CO_2 adsorbed on the MSN and NiM catalysts in the region of 1800–1400 cm^{-1}. For MSN, two prominent peaks were observed at 1631 and 1470 cm^{-1}, which are attributed to symmetric and asymmetric O—C—O stretching modes of bidentate carbonates, respectively [30]. Compared to the MSN, the intensity of these peaks was increased for the NiM catalysts, and the highest intensity was observed for the NiM_IS catalyst. In addition, a new peak around 1538 cm^{-1} appeared for the NiM_IM and NiM_PM catalysts and at 1550 and 1520 cm^{-1} for NiM_IS, which could be attributed to unidentate carbonates associated with stronger basic sites [31]. It is known that the formation of unidentate and bidentate carbonates requires surface basic oxygen atoms, for which unidentate carbonates are formed by CO_2 dissociation with strong basic sites and bidentate carbonates are formed by CO_2 adsorption at medium strength basic sites [32]. Therefore, the addition of Ni into the MSN catalysts, irrespective of the preparation method, increased the concentration and strength of the basic sites on the surface of the catalysts. Among the three NiM catalysts, the highest concentration of bidentate carbonate was observed on NiM_IS, followed by NiM_PM and NiM_IM. However, a different trend was observed for the concentration of unidentate carbonate (NiM_PM > NiM_IS > NiM_IM). In conclusion, NiM_IS possessed the highest concentration of total basicity, which could be attributed to the co-existence of Ni_2O_3 species and abundant silanol groups generated from desilication. Therefore, it can be stated that the structure defect and basic sites can be dedicated as the active sites for CO_2 activation.

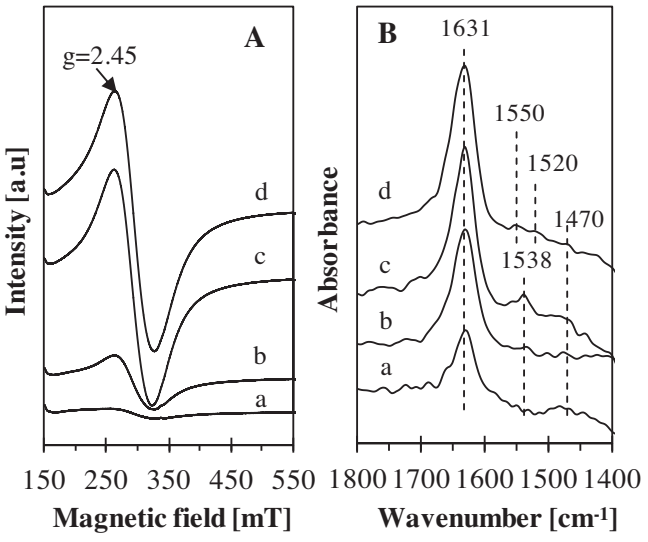

Fig. 7. (A) ESR and (B) CO_2 adsorbed IR of (a) MSN, (b) NiM_IM, (c) NiM_PM and (d) NiM_IS catalysts.

3.2. Catalytic testing

The initial activity of the catalysts in CO_2 reforming of CH_4 was studied in the mixed feedstock gases of $CO_2/CH_4/N_2 = 1/1/1$ under atmospheric pressure. A comparative test over the parent MSN was also carried out under the same conditions, showing no significant (less than 5%) conversion of CH_4 and CO_2. The CH_4 and CO_2 conversions of all catalysts at temperatures ranging from 300 to 800 °C are shown in Fig. 8. Conversion of both reactants increased with increasing temperature, which is in accordance with the thermodynamic studies of CO_2 reforming of CH_4 process [33]. At almost all of temperatures studied, NiM_IS exhibited the highest activity for CH_4 and CO_2 conversions compared to the NiM_PM and NiM_IM catalysts. Even at the highest temperature, the conversion of CH_4 for NiM_IM and NiM_PM could not exceed more than 45.6 and 60.5%, respectively, whereas a conversion of up to 94.3% was achieved for CH_4 when using NiM_IS. The rate and turnover frequency (TOF) of CH_4 conversion (Table 3) also increased in the order of NiM_IM < NiM_PM < NiM_IS.

According to the proposed mechanisms for CO_2 reforming of CH_4, the stepwise adsorption of CH_4 followed by its decomposition into CH_x fragments occurs on active metal sites, whereas CO_2 activation occurs mainly over the support [5]. Based on this information, it can be assumed that the excellent catalytic activity

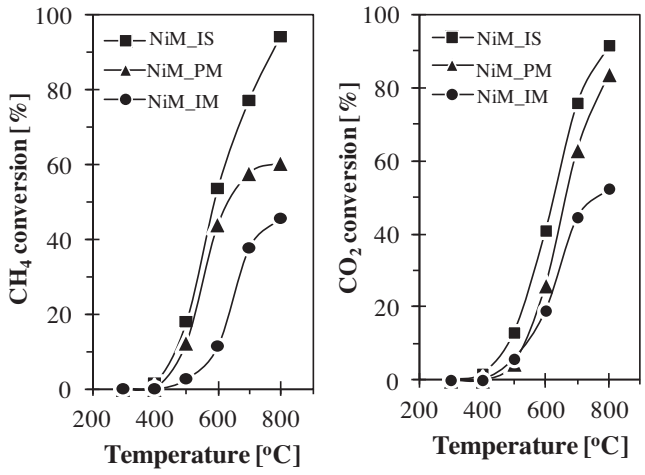

Fig. 8. The catalytic activity of NiM_IS, NiM_PM and NiM_IM catalysts in CO_2 reforming of CH_4.

of NiM_IS is closely associated with the availability of a great number of exposed Ni^0 sites, which are accessible for the reactant molecules. It should be noted that the reduction temperature of all Ni species in NiM catalysts is lower than the temperature of catalyst reduction and the catalytic reaction. Thus, all of the Ni species were reduced to Ni^0 sites under the experimental conditions of the reforming reaction, as proven by the XRD analysis (Fig. 1C). It is well known that a higher density of active metal sites can be achieved by controlling the metal particle size. The H_2 chemisorption results demonstrated a high dispersion of Ni species on the surface of the NiM_IS catalyst. Moreover, XRD analysis showed that the Ni^0 particles with the smallest average size were observed for NiM_IS. An improved dispersion of Ni active sites under in-situ electrolysis conditions might be formed, owing to the existence of a strong interaction between the Ni and the support [34]. From the TPR results it is clear that the strongest Ni-support interaction is established for the NiM_IS catalyst, as expressed by the formation of a large amount of hard-to-reduce Ni species on the surface of the MSN. While the lower catalytic activity of NiM_PM and NiM_IM is attributed to the inferior dispersion of Ni species as well as the larger Ni^0 particles size arose from the weaker Ni-support interaction. Rahemi et al. [35] also found that the morphology and crystallite size are vital factors in enhancing CH_4 conversion. Table 4 shows the comparison of mesoporous silica and alumina-supported Ni catalysts in terms of Ni loading method, Ni loading, NiO particle size and CH_4 conversion [36–42]. It is clearly shown that under the same reaction temperature and with similar supported catalyst structure, our NiM_IS showed a comparable and even higher CH_4 conversion than the supported catalyst reported in literatures even though those reported catalysts have higher metal loadings. Combining the catalytic results and the NiO particle size obtained for various catalysts, it is manifested that smaller NiO particle is beneficial to the catalytic performance. Therefore, it is reasonable to assume that Ni species that are finely dispersed over the MSN support are responsible for the best catalytic behavior of the NiM_IS catalyst. It is believed that the method of introducing Ni plays an important role in controlling the particle size and activity of the catalyst. To the best of our knowledge, the preparation of supported Ni catalysts via in-situ electrolysis is rare, and worth to be explored due to its potential in tailoring the Ni particle size.

The CO_2 conversion of the catalysts increased in the order of NiM_IM < NiM_PM < NiM_IS. At 800 °C, the CO_2 conversion for NiM_IM, NiM_PM, and NiM_IS was 52.4, 83.9, and 91.7% respectively. It should be mentioned that the CO_2 conversion is most likely affected by the basicity of the catalyst. In this study, the highest CO_2 conversions of NiM_IS could be correlated with the medium Lewis basicity of MSN support, which enhances the adsorption and dissociation of CO_2 on the surface of catalyst.

Table 3
Catalytic performances of MSN, NiM_IS, NiM_PM and NiM_IM catalysts.

Catalysts	Reaction rate × 10^{-8} (mol g^{-1} s^{-1})[a]		Conversion (%)[a]		H_2/CO ratio[b]	TOF of CH_4 conversion × 10^{-4} (s^{-1})[c]	Carbon content (%)[d]
	CH_4	CO_2	CH_4	CO_2			
MSN	0.12	0.11	3.72	4.53	0.78	0.08	–
NiM_IS	3.14	2.30	94.3	91.7	1.15	2.11	0.84
NiM_PM	2.01	1.97	60.5	83.9	1.07	1.57	2.35
NiM_IM	1.48	1.17	45.6	52.4	0.91	1.34	2.97

[a] Data at 800 °C.
[b] Data at similar conversion level of CH_4 conversion (45 %), for all catalysts.
[c] Calculated based on mole of CH_4 converted per mole of Ni per second.
[d] Data form TGA analysis on the used catalyst.

Table 4
Comparison of silica and alumina supported Ni catalysts for CO_2 reforming of CH_4.

Catalysts	Method	Ni loading (wt%)	NiO particle (nm)	Reaction temperature (°C)	CH_4 conversion (%)	Ref.
NiM_IS	In-situ electrolysis	5	5.63	800	94.3	This study
NiM_IM	Impregnation	5	12.1	800	45.6	This study
NiM_PM	Physical mixing	5	6.10	800	60.5	This study
Ni/mSiO_2	Sublimation-deposition	10	2.1–4.3	800	~90	[36]
Ni/SiO_2	Amine complexation assisted-wetness impregnation	5	3.8	700	~80	[37]
Ni/mSiO_2	Atomic layer deposition	2.81	n.a	800	52.4	[38]
Ni/mAl_2O_3	Ultrasound assisted-incipient wetness impregnation	5	n.a	800	~97	[39]
Ni/KIT-6	One-pot co-assembly	6	3–5	800	~88	[40]
Ni/SBA-15	Incipient wetness impregnation	12	20.6	800	97.2	[41]
Ni/TUD-1	Grafting	3.83	7.9	800	~78	[42]
Ni/TUD-1	Direct incorporation	3.97	17	800	~55	[42]
Ni/TUD-1	Impregnation	4.24	22	800	~35	[42]

Moreover, it is reported that surface defects can become the centers that capture acidic CO_2 during the reaction [43]. Thus, the presence of a large amount of Ni_2O_3 species in the catalyst also plays a role in enhancing the adsorption of CO_2. Therefore, it is possible that the largest number of basic sites and defect sites of NiM_IS was the main reason for its higher activity in converting CO_2 compared to the other catalysts studied.

The H_2/CO ratio is important for the downstream process. The H_2/CO ratios for all catalysts calculated at 45% CH_4 conversion are also listed in Table 3. The NiM_IS and NiM_PM catalysts reached a H_2/CO ratio greater than 1 whereas NiM_IM catalyst showed H_2/CO ratio lower than 1. The higher value of the H_2/CO ratio (>1) could be attributed to the occurrence of CO disproportionation, which occurred mainly at low temperature (≥600 °C) [44]. However, low H_2/CO values (<1) are attributed to the minor contribution of the reverse water gas shift reaction. The simultaneous occurrence of a reverse water gas shift reaction consumes H_2 and produce extra CO, which lowers the H_2/CO ratio [45].

3.3. Characterization of the spent catalysts

Metal sintering under high temperature may induce deactivation for Ni-based catalyst during the CO_2 reforming of CH_4. In order to determine the stability of the Ni^0 particles during the catalytic testing, the XRD pattern of the spent NiM catalysts was measured. Based on Fig. 9A, no NiO phase is visible from the XRD patterns, indicating that the oxidation of Ni^0 was suppressed under the studied reaction condition. In comparison to the reduced XRD patterns (Fig. 1C), the Ni^0 diffraction peaks were intensified in the spent catalysts, suggesting the occurrence of sintering. Besides, the calculated Ni^0 particle size of the spent catalysts (Table 2) for NiM_IS, NiM_PM and NiM_IM were increased from 8.15, 12.6 and 19.7 nm to 15.3, 22.7, and 29.4, respectively. These results revealed that NiM_PM has the highest Ni^0 sintering degree, followed by NiM_IS and NiM_IM. The XRD patterns of the spent NiM catalysts also exhibited a peak at $2\theta = 26.6°$, which can be assigned to the crystallized graphitic carbon structures (JCPDS 26-1080). The intensity of this peak is the lowest for NiM_IS compared to the other catalysts, indicating a lower carbon formation on the surface of the catalyst.

A quantitative analysis of carbon formation over the spent NiM catalysts was investigated by TGA and the results are shown in Fig. 9B and Table 3. For all catalysts, the weight loss of the carbon residuals followed a two-stage pattern, a first one that slowly develops a broad peak from 300 to 450 °C, and a steeper one at temperatures higher than 600 °C. The weight loss pattern in the TGA profiles indicates that different type of carbonaceous species formed on the catalysts. According to previous report [46], the oxidation of amorphous species occurs at low temperature (400–500 °C), while graphite carbon is oxidized at high temperature (above 500 °C). The amount of carbon deposited on the surface of the catalysts was quantified based on the percentage of total weight loss from 400 °C and above. It is clearly exhibited that the NiM_IM has higher carbon content (2.97%) compared to the NiM_PM (2.35%) and NiM_IS (0.84%).

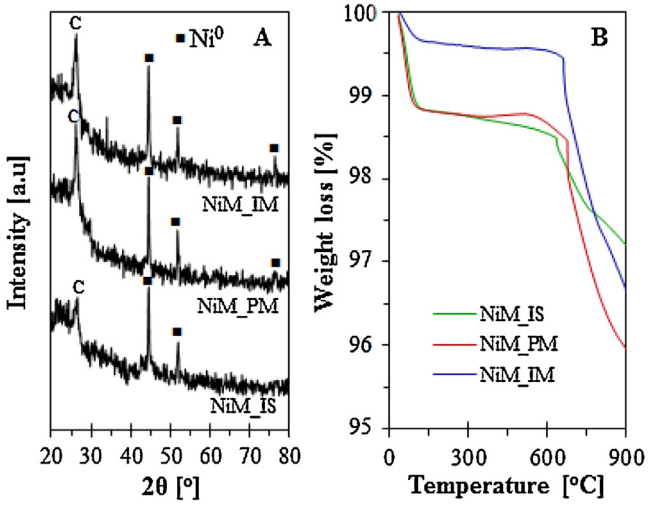

Fig. 9. (A) XRD patterns and (B) TGA profiles of spent NiM_IS, NiM_PM and NiM_IM catalysts.

According to the above analysis, the NiM_IS showed the best catalytic performance and lowest carbon content, which can be ascribed to its high coke resistance. This phenomenon can be explained by the strong metal-support interaction, high basicity and small metallic particles. In this study, the NiM_IS has stronger metal-support interaction as compared to the NiM_IM and NiM_PM, which can be seen from the H_2-TPR results. It is believed that the strong metal-support interaction prevents the Ni^0 particle being carried away from the MSN surface, thus minimizing the growth of encapsulating graphite carbon. While, in a weak metal-support interaction, the Ni^0 particle was easily lifted from the support and prone to the sintering and encapsulated with graphite carbon layer [47].

In addition, the ability of resistance to carbon deposition of the NiM_IS catalyst is related to the property of CO_2 adsorption and activation. In a high CH_4 conversion conditions, carbon formation from CH_4 cracking overwhelmed carbon elimination, and this enables the formed carbon intermediates to develop further towards the formation of long-ranged crystallized structure, which will lead to the higher intensity of graphite in the XRD peak and greater weight loss in TGA profile. The carbon species formed on the support and on the metal were removed by reaction with adsorbed surface CO_2 and adsorbed oxygen species [48]. The ESR and CO_2 adsorbed IR analyses showed that the NiM_IS catalyst has higher number of surface defects and basic sites. Therefore, there will be a higher surface coverage of adsorbed CO_2 which lead to an increase in the rate of carbon gasification and lower rate of carbon formation. It indicated that the ability of coking resistivity is directly correlated with the basicity of the NiM_IS catalyst.

Another advantage of the NiM_IS catalyst is the small size of Ni^0 particles. In the previous research, many investigators have reported the metallic particle size was a critical factor to inhibit carbon formation. It is pointed out that the rate of carbon formation can be controlled when the metallic particle size are/or below 10 nm [49]. A previous report suggested that the activation of CO_2 is structure-sensitive, and small particle size of Ni^0 prompted its activation [50]. The smaller Ni^0 particles are beneficial in promoting the migration of the carbon intermediates to the Ni-MSN interface, and increased the reaction between lattice oxygen and the carbon residuals, thus reduced the carbon formation.

4. Conclusions

In this study, a series of NiM catalysts were prepared from an electrolyzed Ni precursor using physical mixing (NiM_PM), impregnation (NiM_IM), and in-situ electrolysis (NiM_IS) methods. We found that the different Ni-loading methods led to different structures and performances of NiM catalysts. The additions of Ni decreased the surface area and pore volume of all of the NiM catalysts, owing to pore blockage. Depending on the preparation method, NiM catalysts with average Ni^0 crystallite sizes of 8–20 nm were prepared. The size of the Ni crystallite size was found to be dependent on the metal-support interaction during the preparation of the catalyst. The introduction of Ni into

NiM_IM and NiM_IS resulted in a lower reducibility compared to NiM_PM, owing to the formation of Si—O—Ni bonds through sequential desilication–substitution during the catalyst preparation. NiM_IS and NiM_PM possessed a higher Ni_2O_3 species, whereas NiM_IM contained a dominant NiO species. The presence of Ni_2O_3 was beneficial to improve the concentration of the basic sites and structure defects in the catalysts, thus increasing the amount of active sites available for CO_2 activation. The NiM_IS catalyst exhibited the highest catalytic activity and H_2 selectivity as well as the lowest carbon content among the three catalysts, owing to its stronger metal-support interaction, smaller Ni^0 crystallite size, and higher number of structure defects and basic sites. The combination of the good dispersion and small size of the Ni^0 particles with the high concentration basicity and surface defects in the NiM_IS catalyst constitutes its potential as a promising catalyst in renewable hydrogen production.

Acknowledgements

This work is supported by the Universiti Teknologi Malaysia through Research University Grant no. 05H09. Our gratitude also goes to the Ministry of Higher Education (MOHE) Malaysia for the award of MyPhD Scholarship (Siti Munirah Sidik) and the Hitachi Scholarship Foundation for the Gas Chromatograph Instrument Grant.

References

[1] S. Sengupta, G. Deo, J. CO_2 Util. 10 (2015) 66–77.
[2] D.S. Llobet, J.L. Pinilla, R. Moliner, I. Suelves, Fuel 139 (2015) 71–78.
[3] A.I. Paksoy, B.S. Caglayan, A.E. Aksoylu, Appl. Catal. B Environ. 168 (2015) 164–174.
[4] G. Mahoney, J.M. Pusel, S.M. Stagg-Williams, S. Faraji, J. CO_2 Util. 6 (2014) 40–44.
[5] Y. Vafaeian, M. Haghighi, S. Aghamohammadi, Energy Convers. Manag. 76 (2013) 1093–1103.
[6] S.M. Sidik, A.A. Jalil, S. Triwahyono, T.A.T. Abdullah, A. Ripin, RSC Adv. 5 (2015) 37405–37414.
[7] M. Arsalanfar, A.A. Mirzaei, H.R. Bozorgzadeh, Ind. Eng. Chem. 19 (2013) 478–487.
[8] N.H.N. Kamarudin, A.A. Jalil, S. Triwahyono, R.R. Mukhti, M.A.A. Aziz, H.D. Setiabudi, M.N.M. Muhid, H. Hamdan, Appl. Catal. A Gen. 431 (2012) 104–112.
[9] N.W.C. Jusoh, A.A. Jalil, S. Triwahyono, A.H. Karim, N.F. Salleh, N.H.R. Annuar, N. F. Jaafar, M.L. Firmansyah, R.R. Mukhti, M.W. Ali, Appl. Surf. Sci. 330 (2015) 10–19.
[10] R. Jusoh, A.A. Jalil, S. Triwahyono, N.H.N. Kamarudin, RSC Adv. 5 (2015) 9727–9736.
[11] N.W.C. Jusoh, A.A. Jalil, S. Triwahyono, C.R. Mamat, Appl. Catal. A Gen. 492 (2015) 169–176.
[12] A.H. Karim, A.A. Jalil, S. Triwahyono, S.M. Sidik, N.H.N. Kamarudin, R. Jusoh, N. W.C. Jusoh, B.H. Hameed, J. Colloid Interface Sci. 386 (2012) 307–314.
[13] M.A.A. Aziz, A.A. Jalil, S. Triwahyono, R.R. Mukhti, Y.H. Tuafiq-Yap, M.R. Sazegar, Appl. Catal. B Environ. 147 (2014) 359–368.
[14] A.A. Jalil, N. Kurono, M. Tokuda, Tetrahedron 58 (2002) 7477–7484.
[15] S. Damyanova, B. Pawelec, K. Arishtirova, J.L.G. Fierro, C. Sener, T. Dogu, Appl. Catal. B Environ. 92 (2009) 250–261.
[16] P.P. Upare, M.G. Jeong, Y.K. Hwang, D.H. Kim, Y.D. Kim, D.W. Hwang, U.H. Lee, J. S. Chang, Appl. Catal. A Gen. 491 (2015) 127–135.
[17] M.R. Sazegar, A.A. Jalil, S. Triwahyono, R.R. Mukhti, M. Aziz, M.A.A. Aziz, H.D. Setiabudi, N.H.N. Kamarudin, Chem. Eng. J. 240 (2014) 352–361.
[18] E. Lovell, Y. Jiang, J. Scott, F. Wang, Y. Suhardja, M. Chen, J. Huang, R. Amal, Appl. Catal. A Gen. 473 (2014) 51–58.
[19] C.W. Hu, J. Yao, H.Q. Yang, Y. Chen, A.M. Tian, J. Catal. 166 (1997) 1–7.
[20] T.F. Silva, J.A.C. Dias, C.G. Maciel, J.M. Assaf, Catal. Sci. Technol. 3 (2013) 635–643.
[21] H. Ji, T. Wang, M. Zhang, Y. She, L. Wang, Appl. Catal. A Gen. 282 (2005) 25–30.
[22] G.R. Moradi, M. Rahmanzadeh, F. Khosravian, J. CO_2 Util. 6 (2014) 7–11.
[23] P. Turlier, H. Praliaud, P. Moral, G.A. Martin, J.A. Dalmon, Appl. Catal. 19 (1985) 287–300.
[24] M. Iwamoto, Molecules 16 (2011) 7844–7863.
[25] A.S. Lotina, L. Daza, Appl. Catal. A Gen. 474 (2014) 107–113.
[26] A. Jentys, J.A. Lercher, in: H.V. Bekkum, E.M. Flanigen, P.A. Jacobs, J.C. Jansen (Eds.), Studies in Surface Science and Catalysis 137, Elsevier Science, 2001, pp. 345–385.
[27] J.L. Ewbank, L. Kovarik, C.C. Kenvin, C. Sievers, Green Chem. 16 (2014) 885–896.
[28] M. Ivanovskaya, P. Bogdanov, Sensors Actuators B Chem. 53 (1998) 44–53.
[29] K.S. Kim, R.E. Davis, J. Electron. Spectrosc. 1 (1972) 251–258.
[30] E.M. Köck, M. Kogler, T. Bielz, B. Klötzer, S. Penner, J. Phys. Chem. C 117 (2013) 17666–17673.
[31] S.C. Shen, X. Chen, S. Kawi, Langmuir 20 (2004) 9130–9137.
[32] M.B. Jensen, S. Morandi, F. Prinetto, A.O. Sjastad, U. Olsbye, G. Ghiotti, Catal. Today 197 (2012) 38–49.
[33] L. Qian, W. Cai, L. Zhang, L. Ye, J. Li, M. Tang, B. Yue, H. He, Appl. Catal. B Environ. 164 (2015) 168–175.
[34] L. Mo, K.K.M. Leong, S. Kawi, Catal. Sci. Technol. 4 (2014) 2107–2114.
[35] N. Rahemi, M. Haghighi, A.K. Babaluo, S. Allahyari, M.F. Jafari, Energy Convers. Manag. 84 (2014) 50–59.
[36] T. Xie, X. Zhao, J. Zhang, L. Shi, D. Zhang, Int. J. Hydrogen Energy 40 (2015) 9685–9695.
[37] X.Y. Gao, J. Ashok, S. Widjaja, K. Hidajat, S. Kawi, Appl. Catal. A Gen. 503 (2015) 34–42.
[38] D.H. Kim, J.K. Sim, J. Lee, H.O. Seo, M.G. Jeong, Y.D. Kim, S.H. Kim, Fuel 112 (2013) 111–116.
[39] L. Xu, H. Zhao, H. Song, L. Chou, Int. J. Hydrogen Energy 37 (2012) 7497–7511.
[40] Z. Liu, J. Zhou, K. Cao, W. Yang, H. Gao, Y. Wang, H. Li, Appl. Catal. B Environ. 125 (2012) 324–330.
[41] T. Huang, W. Huang, J. Huang, P. Ji, Fuel Process. Technol. 92 (2011) 1868–1875.
[42] X.Y. Quek, D. Liu, W.N.E. Cheo, H. Wang, Y. Chen, Y. Yang, Appl. Catal. B Environ. 95 (2010) 374–382.
[43] C. Drouilly, J.M. Krafft, F. Averseng, H.L. Pernot, D.B. Bachi, C. Chizallet, V. Lecocq, G. Costentin, Appl. Catal. A Gen. 453 (2013) 121–129.
[44] X. Lin, R. Li, M. Lu, C. Chen, D. Li, Y. Zhan, L. Jiang, Fuel 162 (2015) 271–280.
[45] D. Pakhare, C. Shaw, D. Haynes, D. Shekhawat, J. Spivey, J. CO_2 Util. 1 (2013) 37–42.
[46] I.H. Son, S.J. Lee, I.Y. Song, W.S. Jeon, I. Jung, D.J. Yun, D.-W. Jeong, J.-O. Shim, W.-J. Jang, H.-S. Roh, Fuel 136 (2014) 194–200.
[47] T. Huang, W. Huang, J. Huang, P. Ji, Fuel Process. Technol. 92 (2011) 1868–1875.
[48] L. Qian, Z. Ma, Y. Ren, H. Shi, B. Yue, S. Feng, J. Shen, S. Xie, Fuel 122 (2015) 47–53.
[49] J. Zhang, H. Wang, A.K. Dalai, Appl. Catal. A Gen. 339 (2008) 121–129.
[50] D. Li, L. Wang, M. Koike, Y. Nakagawa, K. Tomishige, Appl. Catal. B Environ. 102 (2011) 528–538.